ACS MATERIALS Au
AN OPEN ACCESS JOURNAL OF THE AMERICAN CHEMICAL SOCIETY

pubs.acs.org/materialsau
Article

Phase Segregation Mechanisms in Mixed-Halide $CsPb(Br_xI_{1-x})_3$ Nanocrystals in Dependence of Their Sizes and Their Initial [Br]:[I] Ratios

Hannah Funk, Tal Binyamin, Lioz Etgar, Oleksandra Shargaieva, Thomas Unold, Alberto Eljarrat, Christoph T. Koch, and Daniel Abou-Ras*

Cite This: ACS Mater. Au 2023, 3, 687−698
Read Online

ACCESS | Metrics & More | Article Recommendations | Supporting Information

ABSTRACT: Phase segregation in inorganic $CsPb(Br_xI_{1-x})_3$ nanoparticles (NPs) exhibiting originally a homogeneous [Br]:[I] mixture was investigated by means of in situ transmission electron microscopy (TEM) and evaluated by using multivariate analyses. The colloidal synthesis of the NPs offers good control of the halide ratios on the nanoscale. The spatially resolved TEM investigations were correlated with integral photoluminescence measurements. By this approach, the halide-segregation processes and their spatial distributions can be described as being governed by the interaction of three partial processes: electron- and photon-irradiation-induced iodide oxidation, local differences in band gap energy, and intrinsic lattice strain. Since the oxidation can be induced by both electron-beam and light irradiation, both irradiation types can induce phase segregation in $CsPb(Br_xI_{1-x})_3$ compounds. This makes in situ TEM a valuable tool to monitor phase transformation in corresponding NPs and thin films on the sub-nm scale.

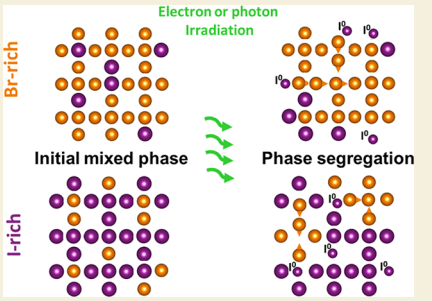

KEYWORDS: *mixed-halide perovskite nanocrystals, transmission electron microscopy, phase segregation, in situ monitoring, multivariate analysis*

1. INTRODUCTION

Inorganic lead-halide-perovskite (LHP) with the stoichiometry $A^+B^{2+}X^-_3$ (A^+ = formamidinium (FA^+), methylammonium (MA^+), Cs^+; B^{2+} = Pb^{2+}, Sn^{2+}; X^- = Cl^-, Br^-, I^-) exhibits an exceptional combination of optoelectronic properties: a sharp, optical absorption onset, low, nonradiative recombination rates, and high open-circuit voltages.[1] Furthermore, the band gap energy is tunable over a range from 1.15 to 3.06 eV by interchanging and mixing A^+ cations, B^{2+}, and X^- halides.[2] The possibility to design semiconductors with band gap energies of about 1.8 to 2.0 eV makes LHPs very suitable as functional layers in light-emitting diodes (LEDs) and as top cell absorbers in tandem solar cells. The perovskite absorber layer in such tandem devices can be composed of, e.g., $Cs_{0.05}(FA_{0.77}MA_{0.23})_{0.95}Pb(I_{0.77}Br_{0.23})_3$, mixing the organic compounds FA^+ and MA^+ with the inorganic ions Cs^+ and Pb^{2+} and the halides I^- and Br^-. Such tandem devices have reached power conversion efficiencies of above 33%.[3,4]

Nevertheless, the available band gap energies are limited by photoinduced halide phase segregation, a widely reported phenomenon that is not entirely understood that is attributed to be the cause for voltage losses in corresponding solar cells.[5−8] Various models have been discussed for the redistribution of the mobile halides focusing on the influence of (i) differences in band gap energy,[9,10] (ii) polaron-induced lattice strain,[11,12] (iii) carrier gradients,[13] or (iv) lattice strain due to different bonding lengths.[14,15] All models agree in terms of that under equilibrium conditions, the entropic preference of $APbX_3$ is halide mixing and that the process is reversible as long as the system is enclosed.[9,11,13]

Conclusively, more than one of these possible causes may be relevant at the same time. Instead of dividing the different aspects, we can classify them as processes driven by the minimization of the Gibbs free energy. Again, others observe a dynamic staged segregation.[16,17] Illuminating the system deposits energy into it, which, in turn, may cause phase segregation. The phase segregation is determined by how much the illumination changes the kinetic and thermodynamic properties of the material.[18]

Furthermore, the loss of iodide, usually in the form of I_2 or I_3^-, induced by light or chemical hole injection has been widely reported for mixed bromide/iodide perovskites that are not enclosed (for example nanoparticles, NP, or thin films in contact with a solvent).[19−21] Recent publications describe halide oxidation and lead reduction (redox: $2I^- + Pb^{2+} \rightarrow I_2 +$

Received: July 3, 2023
Revised: August 11, 2023
Accepted: August 14, 2023
Published: September 6, 2023

Pb^0) induced by charge carriers as the underling process for halide segregation.[22−26] Other authors refer to it more cautiously as the consequence of hole localization that neutralizes iodide locally.[27] As long as the iodide is still in the system, it is possible for these redox reactions to occur in the opposite direction, which is why the effect is reversible in some cases.

The main method used in the present work to investigate LHPs is transmission electron microscopy (TEM). Electron microscopy is an appropriate tool to obtain and correlate spatially resolved information on morphology, structure, chemical composition, or even band gap energies. However, LHPs and especially organic LHPs are very electron-beam sensitive.[28] The present work will therefore focus on the less sensitive inorganic cesium lead-halide perovskites. Also, for $CsPbX_3$, it is crucial to know about the effects of the electron-beam irradiation to correctly characterize the material. Generally, an electron beam can cause (a) atomic displacement (knock-on damage), (b) radiolysis (ionization of material), i.e., losses between a few eV for excitation of conduction or valence electrons and tens or hundreds of eV for ionization of inner atomic shells, (c) creation of excitons (band transitions in the material), and (d) generation of phonons/heating in the investigated material. Detailed theory of the different interaction processes and their scattering cross-sections can be found in publications by Egerton et al.[29−34] Dang et al. investigated experimentally the electron-beam damage in LHPs in detail[35−37] and applied Egerton's interaction theory to halide perovskites.[38] From Dang's work and also from the work by other authors,[39−41] it has been established that radiolysis is the main damage process for electron irradiation in LHP. Since radiolysis is dominant at low electron-beam voltages,[42] higher electron beam voltages are less harmful to LHPs.[36,41] Furthermore, it is rather the total electron dose that is critical compared to the dose rate.[43] For organic as well as for inorganic LHPs, the decomposition into PbX_2 (X = I, Br, Cl) and metallic Pb has been reported by various authors.[36,40,44−47] Due to the similar atomic interplanar distances of $APbX_3$, PbX_2, and Pb, decomposition products are often wrongly identified as perovskites in the literature.[48,49]

We would like to note that although energy-dispersive X-ray or electron energy-loss spectroscopy are established techniques for the study of elemental distributions in NPs on the (sub-)nm scale, these methods have never been successfully applied to the in situ monitoring of phase segregation in mixed-halide perovskite NPs. Therefore, only results from TEM imaging are shown and evaluated in the present work. Moreover, the presented TEM approach is not a high-throughput method, i.e., only a few nanoparticles can be investigated effectively. This fact contrasts with photoluminescence (PL) spectroscopy, which has been applied broadly to investigate phase segregation in nanocrystals. While these investigations are scientifically sound, the authors lacked the means to detect spatial phase distributions in nanocrystals due to the absence of high-resolution microscopy in their methods.

The present work reports about halide phase segregation in colloidal nanocrystals of mixed-halide $CsPb(Br_xI_{1-x})_3$ in dependence on their sizes and initial halide ratios [Br]:[I] and provides further confirmation that halide oxidation indeed plays a key role in halide segregation. The phase segregation was induced and monitored in situ by high-resolution TEM (HRTEM) on the sub-nm scale and evaluated by multivariate analysis (MA). Furthermore, the results were correlated with light-induced phase segregation monitored by PL spectroscopy. For the discussion, the findings of the present work were compared with the findings of a previous study by Funk et al.[50,51]

2. EXPERIMENTAL METHODS

2.1. Sample Synthesis

Chemicals: cesium carbonate (Cs_2CO_3, 99.9%, Sigma-Aldrich), lead(II) bromide ($PbBr_2$, ≥98%, Sigma-Aldrich), lead(II) iodide (PbI_2 99.99%, Sigma-Aldrich), oleic acid (OA, 90%, Sigma-Aldrich), oleylamine (OLAM, 70%, Sigma-Aldrich), 1-octadecene (ODE, 90%, Sigma-Aldrich), ethyl acetate (≥99.5%, Sigma-Aldrich), and hexane (technical grade, Bio-lab) were used as received, without any further purification.

2.1.1. Step 1: Preparation of Cs-Oleate. The Cs-oleate precursor was prepared according to a previously published procedure by Protesescu et al.[52] and by us. In a 100 mL 3-neck flask, 0.6 mmol (0.2 g) of Cs_2CO_3 was mixed with 625 μL of oleic acid (OA) and 7.5 mL of 1-octadecene (ODE). The solution was degassed for 1 h under vacuum conditions at 120 °C and then heated up to 150 °C under Ar flow.

2.1.2. Step 2: Synthesis of $CsPb(Br_xI_{1-x})_3$ (X = Br, I) NPs. The NPs were synthesized according to a previous report.[52] First, different ratios of $PbBr_2$ and PbI_2 (for x = 0.8, 0.4) to a total of 0.188 mmol (0.0552 g of $PbBr_2$ and 0.0172 g of PbI_2 for x = 0.2) were mixed with 0.3 mL of OA, 0.3 mL of OLA, and 5 mL of ODE in an additional 100 mL 3-neck flask. The solution was degassed for 1 h under vacuum at 120 °C and then heated up to 150 °C for small NPs and up to 170 °C for bigger NPs under Ar flow. The reaction was carried out by injecting 0.4 mL of the Cs-oleate precursor solution into the PbX_2 precursor solution. The reaction was quenched using an ice bath after a few seconds. Ethyl acetate was added to the crude solution in a volume ratio of 3:1, and the NPs were centrifuged at 6000 rpm for 10 min. The precipitate was dispersed in hexane for further characterization.

2.2. Structural Characterization

Time series in transmission electron microscopy: TEM imaging was performed using a JEOL JEM2200FS and a 1k slow-scan charge-coupled device (CCD) camera (MSC, Gatan Inc.) at room temperature using electron dose rates given in Table S6 and an accelerating voltage of 200 kV. The electron beam was not blanked at any instant during each time series. The magnification was calibrated using a Si wafer. It should be noted that reversibility of the phase-segregation process cannot be investigated by TEM analyses since further transformations happening in the electron beam right after the phase-segregation process result in the irreversible destruction of the nanoparticles.

2.3. Multivariate Analysis (MA)

Evaluation of TEM time series with multivariate analysis: The two methods used to evaluate a stack of high-resolution TEM images are principal component analysis (PCA) followed by an independent component analysis (ICA).[53,54] While PCA uses a reduction of the dimensionality to simplify the problem at hand, ICA postulates the independence of the source variables. ICA is a special case of a blind source separation and is widely used in digital image processing. For more details on this approach, the reader is referred to refs 50 and 55.

2.4. Photoluminescence Measurements

PL spectra for drop-cast NPs with side lengths of 20−100 nm were acquired by a 1/2 m grating monochromator coupled with a CCD detector. The investigated samples were excited by means of a diode laser emitting light at a wavelength of λ = 409 nm (a spot radius of approx. 100 μm and excitation intensity in the range of 0.3−1.9 W cm^{-2}). The same conditions were used for the drop-cast NPs with side lengths of 20−100 nm. PL spectra of the NPs with a side length of 10−22 nm in solution were measured using an optical flame spectrometer from Ocean Optics and excited by means of an

https://doi.org/10.1021/acsmaterialsau.3c00056
ACS Mater. Au 2023, 3, 687−698

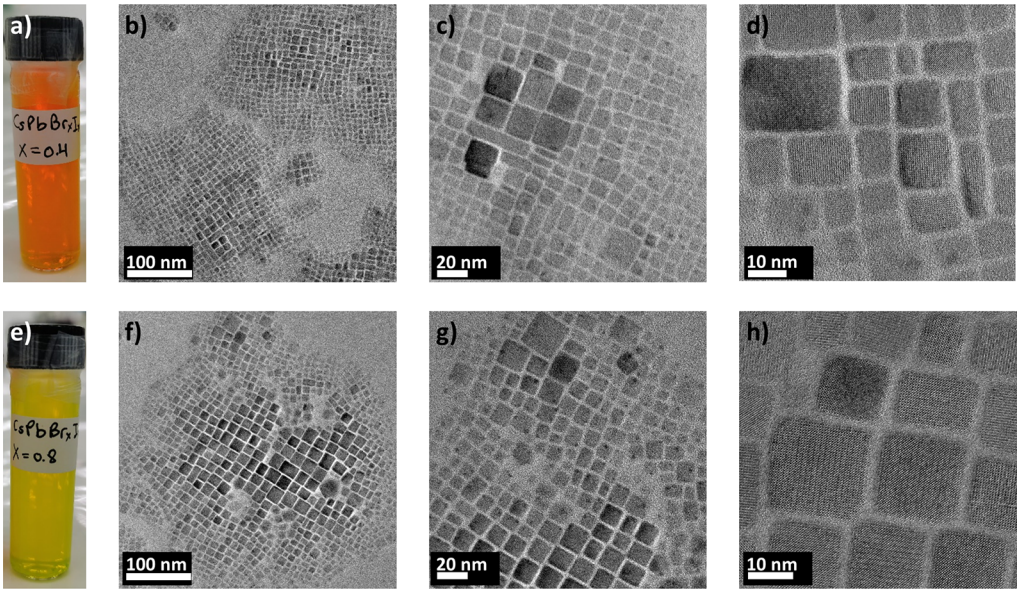

Figure 1. (a) Iodide-rich $CsPb(Br_{0.4}I_{0.6})_3$ NPs (orange) and (e) bromide-rich $CsPb(Br_{0.8}I_{0.2})_3$ NPs (yellow) dispersed in hexane. The tunability of the band gap energy is highlighted by the different colors of these solutions. (b–d) TEM images acquired at various magnifications showing $CsPb(Br_{0.4}I_{0.6})_3$ NPs as well as $CsPb(Br_{0.8}I_{0.2})_3$ NPs in (f–h). The particle side lengths vary between about 10 and 22 nm.

ultraviolet-LED lamp (λ_{max} = 365 nm) at an intensity of about 1 sun (1 kW/m^2) in a N_2 atmosphere. The excitation light was cut band limited using a short-pass filter at 500 nm.

3. RESULTS

3.1. Size Dependence of Phase Segregation in Mixed-Halide NPs

NPs of the composition $CsPb(Br_{0.4}I_{0.6})_3$ and $CsPb(Br_{0.8}I_{0.2})_3$ were synthesized by colloidal synthesis. This process ensures a better control of the iodide/bromide ratio on all scales compared with spin-coated samples and allows for comparability of the results obtained by HRTEM and by integral PL spectroscopy.

Figure 1a,e shows the NPs dispersed in hexane. They exhibit the typical bright orange and yellow colors for iodide-rich and bromide-rich $CsPb(Br_xI_{1-x})_3$, visualizing the tunability of the band gap energy via the [Br]:[I] ratio. The band gap energies were determined to be around 2.23 (556 nm) for $CsPb(Br_{0.4}I_{0.6})_3$ and 2.38 eV (520 nm) for $CsPb(Br_{0.8}I_{0.2})_3$ by PL and absorption spectroscopy as depicted in Figure S1. These values are in good agreement with those reported in the literature[7,21,52,56−59] given in Table S1.

The NPs were drop-cast on a carbon-coated TEM grid, where they assembled in clusters. The larger particles are usually found in the center of a cluster. They are mostly of cubic shape and vary in side length between 10 and 22 nm for both the iodide-rich and the bromide-rich NPs (see Figure 1b–d,f–h).

3.1.1. In Situ TEM Results. HRTEM time series were acquired over a duration of up to 20 min on iodide-rich $CsPb(Br_{0.4}I_{0.6})_3$ and bromide-rich $CsPb(Br_{0.8}I_{0.2})_3$ NPs to monitor electron-beam-induced phase segregation. No such phase segregation was detected for the NPs in the various time series. Figure 2a shows the HRTEM time series of $CsPb(Br_{0.8}I_{0.2})_3$ NPs over a period of 17 min. Slight morphological changes are visible. A multivariate algorithm[50,55] was used to identify and map the structural information from the local atomic structure. Several diffraction patterns were acquired

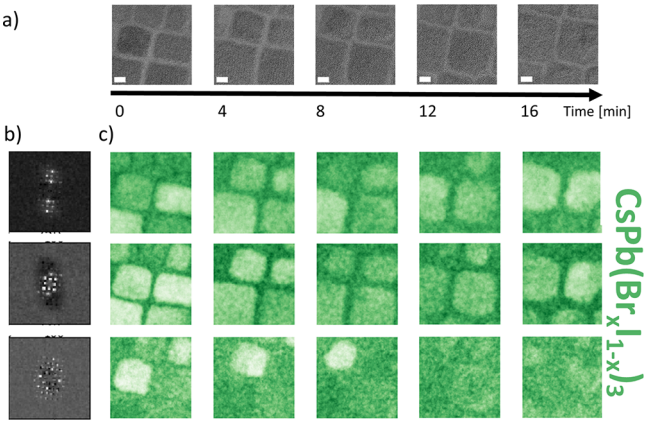

Figure 2. (a) HRTEM images acquired during the 17 min of total acquisition duration (each image 4 min); (b) characteristic diffraction patterns of the several differently orientated structures assigned to $CsPb(Br_{0.8}I_{0.2})_3$; (c) corresponding abundance maps showing no halide phase segregation, but a slow amorphization. High intensity in a pixel corresponds to high abundance of the corresponding diffractogram in that pixel. The scale bar has a length of 5 nm.

during the time series (Figure 2b); all of these patterns were assigned successfully to the $CsPb(Br_{0.8}I_{0.2})_3$ phase by determining the interplanar distances from the reflection positions. The different symmetries of the diffraction patterns can be explained by slightly different crystal orientations of the NPs with respect to the incident electron beam.

In the abundance maps in Figure 2c, a high intensity corresponds to a high abundance of the structure in this pixel. While for phase segregation new phases should appear over time, this is not the case for the small NPs. No new diffraction patterns indicating the evolution of phase segregation or the formation of another phase appear during the time series. The only change observed is that the initial patterns vanish, indicating amorphization. During this process, neither halide phase segregation nor the formation of lead-halide particles

https://doi.org/10.1021/acsmaterialsau.3c00056
ACS Mater. Au 2023, 3, 687−698

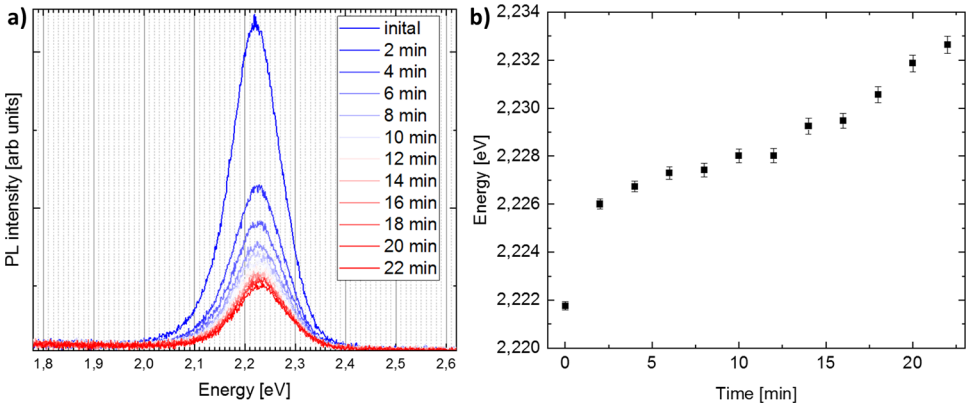

Figure 3. (a) PL intensity of $CsPb(Br_{0.8}I_{0.2})_3$ NPs excited with a white LED lamp over a time period of 22 min. (b) Lorentzian fit of PL peak energy indicating a blue shift of 11 meV (2.7 nm).

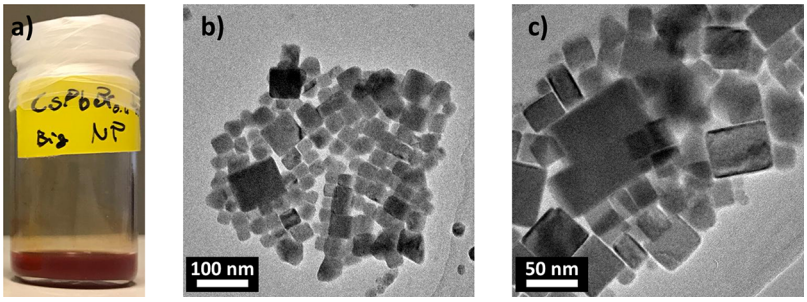

Figure 4. (a) Iodide-rich $CsPb(Br_{0.4}I_{0.6})_3$ NPs (dark red) dispersed in hexane. (b, c) TEM overview images of $CsPb(Br_{0.4}I_{0.6})_3$ NPs with side lengths from 20 to 100 nm.

was observed. Also, in iodide-rich $CsPb(Br_{0.4}I_{0.6})_3$ NPs, no phase segregation was detected.

In spite of the higher magnification and a higher electron dose, the present NPs are much more stable under the electron beam compared to the bigger crystallites of about 40 nm × 40 nm size presented in Funk et al.[50] No phase segregation induced by electron-beam irradiation was observed for iodide-rich $CsPb(Br_{0.4}I_{0.6})_3$ or bromide-rich $CsPb(Br_{0.8}I_{0.2})_3$ NPs of 10−22 nm side lengths. This result is in good agreement with previous PL measurements on $CsPb(Br_xI_{1-x})_3$ NPs that show the absence of phase segregation below a certain NP size.[9,10,21] In the next subsection PL measurements will be correlated with the TEM results and discussed with respect to results in the literature.

3.1.2. In Situ PL Results. Figure 3a shows the PL spectra excited by means of a white LED lamp over a time period of about 22 min. The PL peak does not exhibit a red shift, reported as an indication for halide segregation in bulk material,[5,7,8,13,60] but a blue shift of a few nm was detected for mixed-halide NPs.[9,21] The band gap energy of initially 2.22 eV (559 nm) is in good agreement with the literature and deviates slightly from the value given in Figure S1. This is probably due to another NP concentration in the solution during the measurement since the hexane evaporated during storage and had to be filled up from time to time.

Figure 3b shows the Lorentzian fit of the PL signal in Figure 3a and displays a blue shift of 2.7 nm for 22 min of illumination in an inert atmosphere. A filter effect caused by reabsorption makes the higher energy leg steeper.[61] Therefore, the peak is not symmetric and not strictly Lorentzian, hence, making the fitting error potentially larger than indicated in Figure 3b. However, the tendency is clear and in-line with the literature. Draguta et al.[9] described a 3 nm blue shift after 120 s of excitation (405 nm, I_{exe} = 60 mW cm^{-2}) in $CsPb(Br_{0.5}I_{0.5})_3$. Zhang et al.[21] described an intensity-dependent blue shift in $CsPb(Br_{0.4}I_{0.6})_3$ of 17 nm after 10 min (405 nm, I_{exe} = 30 mW cm^{-2}) and of 115 nm after 80 min (405 nm, I_{exe} = 15 mW cm^{-2}). Furthermore, their measured blue shift is reversible in ensemble films consisting of packed NPs but not reversible in individual NP.[21] The smaller shift in comparison with literature reports detected in the present work may be explained either by the lower intensity of the LED lamp used in the present work or by the inert atmosphere in which the PL measurement was performed.

Both the polaron-based model for halide-phase segregation by Bischak et al.[12] and the band gap-based model by Draguta et al.[9] predict an NP size threshold below which no phase segregation occurs. The polaron-based model rationalizes irradiation-induced lattice vibrations as a possible cause for the halide redistribution. It predicts a minimum size of 8 nm × 8 nm for phase segregation to occur. However, the present work and reports in the literature[9,10] show that phase segregation does not take place in particles with edge lengths of more than 20 nm × 20 nm. In the second model, the band gap differences between I-rich and Br-rich regions cause charge-carrier accumulation in I-rich domains, which again induces the iodide to diffuse to these regions to reduce the free energy. According to the model proposed by Draguta et al.,[9] the segregation rate is dependent on the excitation intensity I_{exc} as well as on the carrier diffusion length $l_{e/h}$. In the case that the particle is smaller than the diffusion length, no phase segregation can occur. This model is supported by the presented results and experiments performed by Gualdrón-Reyes et al.,[10] who reported that, while a blue-shift was

https://doi.org/10.1021/acsmaterialsau.3c00056
ACS Mater. Au 2023, 3, 687−698

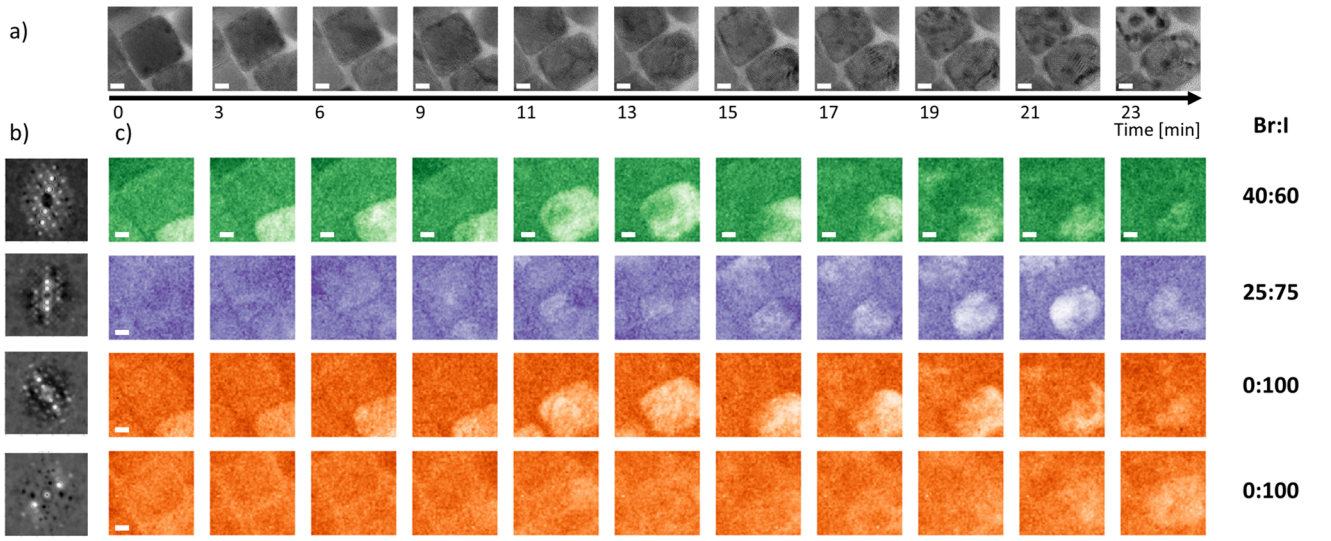

Figure 5. Multivariate analysis of a 40 nm × 45 nm large $CsPb(Br_{0.4}I_{0.6})_3$ crystallite at position A. (a) HRTEM images acquired during 23 min of total acquisition duration, (b) characteristic diffraction patterns of most abundant structures of the upper crystallite, (c) corresponding abundance maps identified as $CsPb(Br_xI_{1-x})_3$ for x = 0.4, 0.25 and 0 (green, purple, and orange). As in Figure 3, a high intensity in a pixel corresponds with a high abundance of the structure in this pixel. The length of the scale bars is 10 nm.

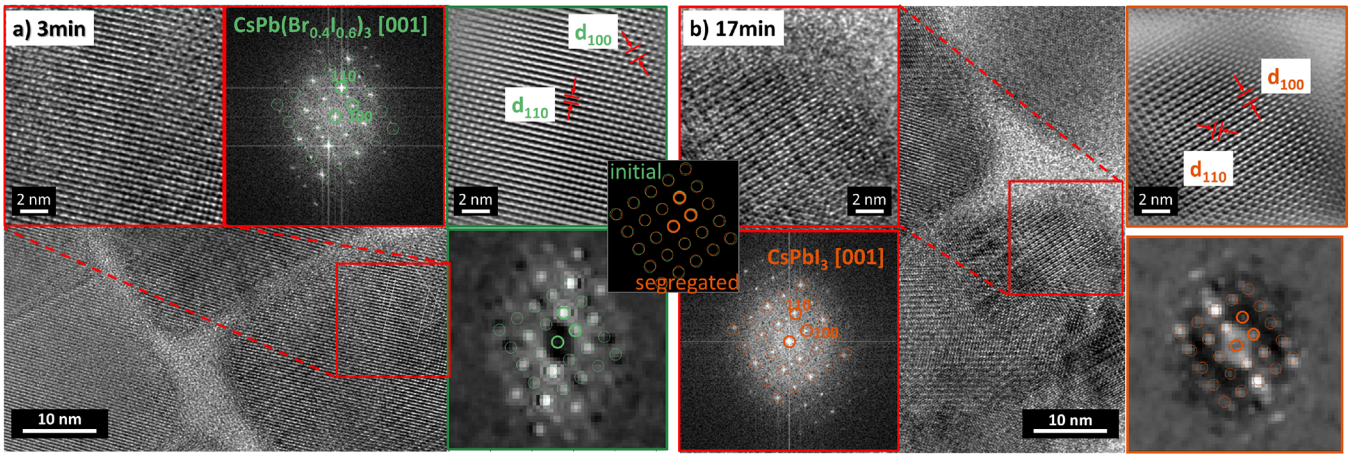

Figure 6. Phases assignment at position A: (a) HRTEM after 3 min and (b) 17 min of electron beam irradiation. For exact phase assignment, the FFT of the image detail (red border) matching the diffraction pattern determined by the MSA algorithm is chosen. The exact interplanar distances are obtained from the Fourier filtered image, for initial $CsPb(Br_{0.4}I_{0.6})_3$ (green) and terminal $CsPbI_3$ (orange). Please note that the zone axes of the crystallites are not perfectly aligned parallel to the incident electron beam.

detected for NPs with a side length of less than about 46 nm, a red-shift was found for NPs with a side length greater than about 46 nm (405 nm, I_{exe} = 10 mW cm^{-2}).

It can be concluded that the TEM results showing no phase segregation are in good agreement with the PL results and those reported in the literature. A shift of 2.7 nm in the PL peak, as observed by PL during 22 min of irradiation, corresponds to a change in lattice parameters that lies below the detection limit of the phase assignment by TEM.

3.2. Spatial Evolution of Phase Segregation in Iodide-Rich Nanoparticles with Side Lengths of >40 nm

As described in the previous subsection, halide segregation is not observable in TEM or PL for small (20−22 nm side length) mixed-halide NPs. However, electron-beam-induced phase segregation for a crystallite with a side length of about 40 nm was indeed observed as described in Funk et al.[50] and photoinduced phase segregation for particles with a side length of 46 nm or larger was reported using PL analysis.[10] These results are explained well by the band gap-based model,[9] which predicts a size threshold below which light-induced phase segregation is not occurring. Hence, $CsPb(Br_{0.4}I_{0.6})_3$ NPs with a wider size distribution were produced by changing the temperature during step 2b of the colloidal synthesis.

Figure 4a shows the solution containing large, iodide-rich $CsPb(Br_{0.4}I_{0.6})_3$ NPs (dark red), in comparison with the small, bromide-rich $CsPb(Br_{0.8}I_{0.2})_3$ (yellow) and iodide-rich $CsPb(Br_{0.4}I_{0.6})_3$ (orange) NPs. As depicted in Figure 4b,c, the iodide-rich particles are mostly of cubic shape, and their side lengths range from about 20 to 100 nm.

3.2.1. In Situ TEM Results. Probing particles with side lengths between 40 and 50 nm at a magnification of 300,000 proved to be the right tradeoff between a high resolution and more or less full view of one crystallite sufficiently large to monitor the halide phase segregation. In the following, halide phase segregation is induced and monitored at two different

https://doi.org/10.1021/acsmaterialsau.3c00056
ACS Mater. Au 2023, 3, 687−698

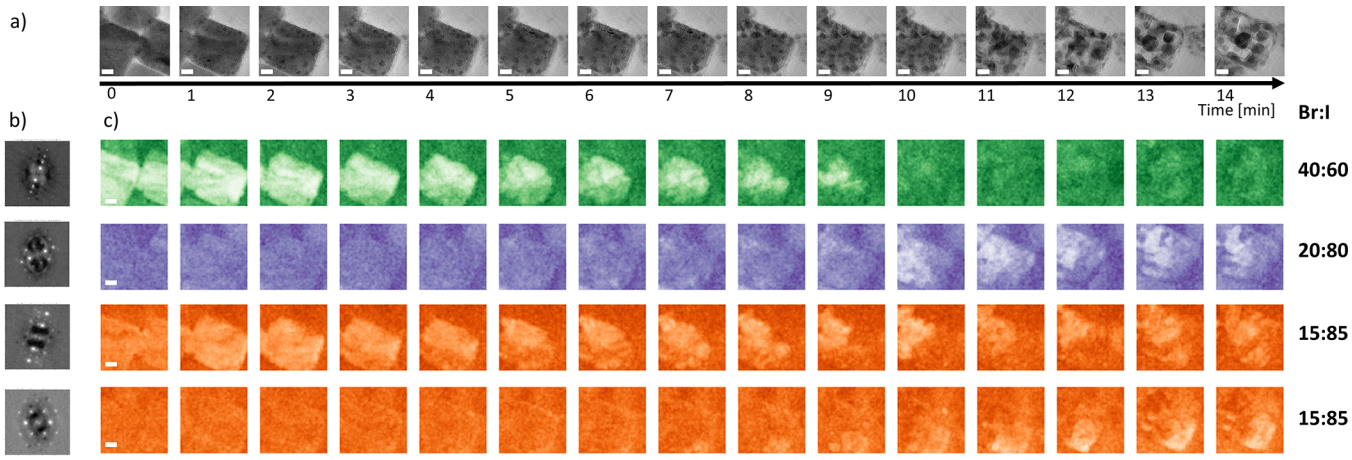

Figure 7. Time series of an initially 40 nm × 50 nm large $CsPb(Br_{0.4}I_{0.6})_3$ crystallite at position B. (a) HRTEM images acquired during 14 min of total acquisition duration; (b) characteristic diffraction patterns of the most abundant structures as identified by multivariate analysis; (c) corresponding abundance maps identified as $CsPb(Br_xI_{1-x})_3$ for x = 0.4, 0.20, and 0.15 (green, purple, and orange). High intensity in a pixel corresponds to a high abundance of the structure in this pixel. Scale bars are 10 nm.

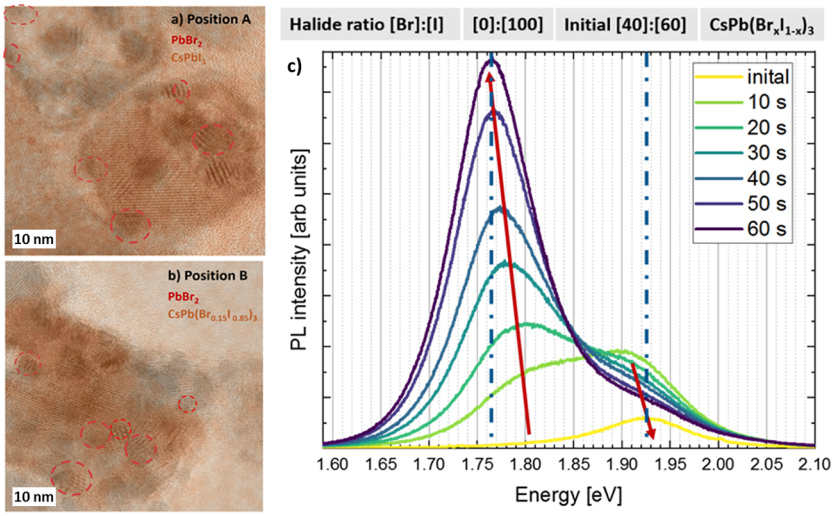

Figure 8. HRTEM image with the overlay of the I-rich ICA abundance map for (a) position A after 23 min and (b) position B after 10 min of electron-beam irradiation. In both time series, inclusions of Br-rich areas are present that can be identified as $PbBr_2$. (c) PL peak intensity of initial $CsPb(Br_{0.4}I_{0.6})_3$ excited with a 409 nm diode laser measured over 1 min. The initial peak red shifts from 1.93 eV (645 nm) correspond to a [Br]:[I] ratio of [40]:[60] toward a stable value of about 1.77 eV (700 nm) corresponding to a ratio of [0]:[100].

positions of the same sample, which will be referred to as position A and position B.

3.2.2. Multivariate Analysis. To analyze the evolution of the electron beam-induced phase segregation in $CsPb(Br_{0.4}I_{0.6})_3$ NPs, multivariate statistical analysis (MSA) was applied to HRTEM time series acquired at different positions of the sample. Figure 5a shows a HRTEM time series recorded at position A over a time period of 23 min. As in the previous section, the algorithm virtually scanned each HRTEM image, collecting the structural information encoded in the FFTs of small patches of the atomic-resolution images. Then, the above mentioned PCA & ICA methods were used to reduce the dimensionality of the data set and to identify the abundant crystalline phases in form of characteristic diffractograms. Figure 5b displays the most abundant components of the diffractograms for the lower particle in the HRTEM images. The abundance maps in Figure 5c display the evolution of the corresponding structure over time. A high contrast pixel in the abundance maps corresponds to a high abundance of the respective structure in this pixel.

The abundance maps in Figure 5c show how the lower particle of initially $CsPb(Br_{0.4}I_{0.6})_3$ (green) transforms into an iodide-richer region of $CsPb(Br_{0.25}I_{0.75})_3$ (purple) as well as into pure $CsPbI_3$ (orange, in two orientations) during the first 12 min, before additional further transformations occur under the electron beam, and the particle decomposes as visible in the HRTEM images. The upper particle in Figure 5 exhibits a very similar segregation behavior as well as the evolution of Pb during the later stages when the particle decomposes visibly but is oriented differently. Its multivariate analysis can be found in Figure S3, and HRTEM results can be found in Figure S4.

The [Br]:[I] ratio of each diffraction pattern was identified by using Vegard's law[62] as well as the cubic lattice parameters of 5.874 Å for $CsPbBr_3$[63] and 6.289 Å for $CsPbI_3$,[64] since the deviations from the actual orthorhombic phase of $CsPbX_3$ NPs at room temperature lie below the detection limit of

https://doi.org/10.1021/acsmaterialsau.3c00056
ACS Mater. Au 2023, 3, 687−698

HRTEM.[65] To obtain a higher resolution, the interplanar distances were determined from the original images, instead of from the more pixelated diffractograms. Figure 6 shows exemplarily how, for each abundant structure, the FFTs generated by the MSA algorithm (green/orange border) were compared with the FFTs of the original image (red border) of a region with a high abundance of the corresponding structure. Then, the interplanar distances were measured in the Fourier filtered HRTEM images (green/orange border). A deviation of about ±5% from the halide ratio results from the spatial resolution and inaccuracy of the image extraction. Hence, the resulting phase assignment is to be understood as a trend of the spatial evolution of phase segregation.

Figure 7 shows a second HRTEM time series and its multivariate analysis at position B on the same TEM grid. While the trend of the phase segregation and the following further transformations leading to decomposition are the same as at position A, both processes happen much faster. After about 5 min, the initial $CsPb(Br_{0.4}I_{0.6})_3$ (green) compound transforms into iodide-richer regions of $CsPb(Br_{0.2}I_{0.8})_3$ (purple) and $CsPb(Br_{0.15}I_{0.85})_3$ (orange). At the same time, high-contrast particles are much more visible at position B, indicating the presence of bromide-rich areas that are not resolved by the multivariate analysis.

3.2.3. Bromide Inclusions. As described in the last subsection, for both positions A and B, the initially I-rich $CsPb(Br_{0.4}I_{0.6})_3$ crystallites developed into pure or almost pure $CsPbI_3$, while no region enriched in bromide was detected by means of PCA/ICA (see Figures 5 and 7). Detailed evaluation of the HRTEM by means of ROI-FFT analysis (see Figures S4 and S5) images shows that bromide-rich areas can be found as inclusions of up to 5 nm in size that are too small to be picked up by the MSA algorithm. Figure 8a,b shows these small bromide-rich inclusions at position A as well as at position B in the I-rich matrix.

Because of the structural similarity of the ternary, the binary, and the pure lead phases (e.g., $CsPbBr_3$, $PbBr_2$, Pb_0), it is not always possible to identify one of these phases unambiguously by means of HRTEM. This is especially true in the case that only one direction of lattice planes is resolved in the TEM images. Due to the mass-thickness contrast effect, small high-contrast areas are usually attributed to $PbBr_2$;[35,37,66] this is probably also the case in the present work. Also, the differences in the interplanar distances are often smaller than the measurement error. A careful evaluation comparing FFTs with simulated electron diffraction patterns of the different phases in question was conducted using the JEMS software.[67] Interplanar distances and phase assignments can be found in Section 1 of the Supporting Information.

3.2.4. Time Scale, Intensity, and Residual Organic Material. It is noteworthy that the time scales of the processes in the time series described above differ substantially. While the halide phase segregation at position A (Figure 5) occurred during the first 12 min, at position B, the phase segregation evolved already during the first 5 min before further transformation started to dominate the process (Figure 7). This means that more than twice the total electron dose was necessary to induce phase segregation at position A, in comparison with the particle at position B. Other particles did not show any phase decomposition during exposure of up to 20 min, while at other positions, the decomposition was so fast under the identical conditions that halide-phase segregation was not possible to be analyzed before the particle decomposed (see Figure S6). As described in detail in Section 2 of the Supporting Information, this different behavior in the electron beam is not related to the shape of the NPs or to other properties of the corresponding crystallite (as, e.g., attached ligands) but dominated by local fluctuations of residual organic material from the solution in which the NPs were dispersed and drop-cast. The electron-beam irradiation can decompose hydrocarbons from the organic material and deposit carbon on the sample. Subsequently, further adsorbates diffuse from the surrounding area into the illuminated area. The carbon acts as a protective layer and impedes the volatilization of halide ions from the sample. The suppression of degradation of LHP by carbon coating has been reported in the literature.[47] These effects vary with the thickness of the carbon layer and, hence, with the available organic material in the environment of the electron beam illuminated area.

In conclusion, the large, I-rich $CsPb(Br_{0.4}I_{0.6})_3$ NPs indeed exhibit electron-beam-induced phase segregation into a pure $CsPbI_3$ matrix with Br-rich inclusions. The time scale and occurrence of this process in TEM are dependent on the amount of residual organic material in the specimen. This result indicates that the phase-segregation process is illumination-intensity dependent as predicted by the band gap-dependent phase-segregation models.[9,13,68] In addition, it is important to be aware of the further transformations that occur under the electron beam after the segregation. These further transformations are facilitated by elevated temperatures.[36] An estimate for electron-beam-induced heating is provided in Section 3 of the Supporting Information.

3.2.5. In Situ PL Results. Figure 8c shows the PL measurement performed on large drop-cast NPs in air. The PL peak redshifts from an initial value of 1.93 eV (645 nm) corresponding to a [Br]:[I] ratio of about 40:60 toward a stable value of about 1.77 eV (700 nm) that can be identified as pure $CsPbI_3$. The peak approximate halide ratio was identified with the literature values presented in Table S1.[5,7,8,13,52,59,60,69]

The red shift and the initial and final values of the PL measurements are in very good agreement with the in situ TEM measurements. Both TEM and PL results indicate that the initially I-rich [Br]:[I] ratio of 40:60 $CsPb(Br_xI_{1-x})_3$ crystallites segregated into pure $CsPbI_3$ (and secondary phases observable by TEM). Even though the differences between light and electron-beam irradiation give rise to different time scales that make it difficult to quantitatively compare the intensities, the present work shows that halide phase segregation can be induced by both electron-beam or photon irradiation.

3.2.6. Side Note on the Terminal [Br]:[I] Ratio for Halide Segregation. For LHP thin films, a terminal [Br]:[I] ratio for iodide-richer phases, below which no halide segregation occurs, is observed experimentally. $CsPb(Br_xI_{1-x})_3$ thin films with [Br]:[I] ratios of higher iodine content than [I]/([Br] + [I]) > 60% are reported to be stable against photoinduced halide-segregation.[7] (For $MAPb(Br_xI_{1-x})_3$, stable ratios of [I]/([Br] + [I]) > 80% are reported.[5]) Brennan et al.[13] gave an overview of the extensive literature on the halide-segregation threshold and proposed explanations. However, none of them can explain conclusively the A cation-independent threshold below which no halide segregation occurs.

In the present work, no [Br]:[I] threshold ratio for phase segregation was found in individual NPs of up to 100 nm. As

https://doi.org/10.1021/acsmaterialsau.3c00056
ACS Mater. Au 2023, 3, 687−698

predicted theoretically,[68] a complete segregation, resulting in a pure $CsPbI_3$ phase and a Br-richer phase, was observed. In light of the threshold-riddle in thin films, the present results are intriguing. Hutter et al. reported that the threshold value can be increased, i.e., more ratios can be stabilized against segregation by applying external physical pressure or chemically compressing the unit cell by integrating smaller Cs^+ cations into a $MAPb(Br_xI_{1-x})_3$ lattice.[15] The absence of neighboring grains and/or the volume-to-surface ratio, i.e., the size of the NPs, are likely to play a role for the absence of a threshold ratio reported in the present work and could serve as a starting point to solve the riddle in thin films to eventually stabilize more band gaps for optoelectronic applications.

4. DISCUSSION

As discussed in detail in Section 3.1, it was shown that halide phase segregation in NPs smaller than 23 nm side length does not take place in TEM or PL as predicted by the band gap-based model[9] for halide phase segregation. In accordance with the literature, the PL peak exhibits a slight blue shift, indicating a slow outgassing of iodide from small $CsPb(Br_{0.8}I_{0.2})_3$ NPs, corresponding to a change in the halide ratio that lies below the identification threshold of HRTEM phase assignment. The results of the present work show that the intensity-dependent size threshold of about 40 nm for photosegregation, as predicted by the band gap model, is also given for electron irradiation. Section 3.2 shows phase segregation initiated by an electron beam in TEM as well as light by PL on the same sample. For both methods, the initially I-rich $CsPb(Br_{0.4}I_{0.6})_3$ crystallites of up to 100 nm side length segregated into pure $CsPbI_3$ and secondary phases observable by TEM. Furthermore, the TEM analyses give insights into the phase segregation on the sub-nm scale in mixed-halide perovskite crystallites of side lengths of 40 to 50 nm.

Figure 9 shows the phase segregation in an iodide-rich crystallite of the present work in comparison with the bromide-rich crystallites from Funk et al.[50] In Figure 9b, a clear direction is observable for the phase segregation in the Br-rich $CsPb(Br_{0.8}I_{0.2})_3$ crystallite. An I-rich phase segregates at the edges of the particle, while a pure $CsPbBr_3$ domain forms at the center. In contrast, the I-rich $CsPb(Br_{0.4}I_{0.6})_3$ sample (Figure 9a) segregates into a pure $CsPbI_3$ matrix with small Br-rich inclusions ($CsPbBr_3$ or $PbBr_2$). The spatial distribution of both phases in the segregated condition is characteristic for the initial ratio. However, both initially bromide-rich and iodide-rich ratios have in common that the main phase forms according to the halide with the larger concentration in the compound. To provide an explanation for this behavior, the following pathway is proposed, which at the same time explains why electron-beam and light irradiation can both trigger phase segregation in LHP compounds.

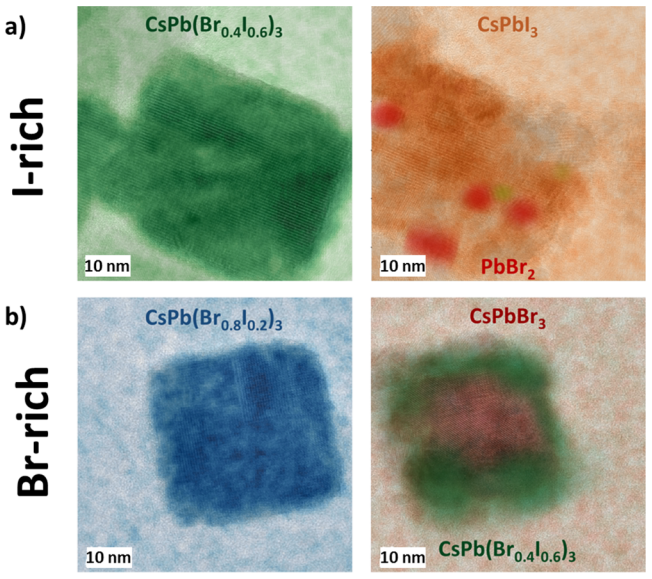

Figure 9. Halide segregation in (a) I-rich and (b) Br-rich crystallites. While the I-rich initial crystallite segregates into $CsPbI_3$ with Br-rich inclusions, the Br-rich initial crystallite segregates into $CsPbBr_3$ a core and an iodide-richer phase at the edges.

4.1. Initiating and Driving Halide Segregation: Interplay of Halide Oxidation, Band Gap Differences, and Lattice Strain

For halide perovskites, radiolysis has been established as the main damaging process when irradiated by an electron beam. Radiolysis can be rationalized as the interaction of the materials electrons with the electromagnetic field of the incoming electrons and causes the oxidation of the halide anion as well as the reduction of the lead cation.[37] As described in the Introduction, the same oxidation process has recently emerged in the halide perovskite community to be the initial step of halide phase segregation induced by light irradiation or by applied voltage. The present work provides further confirmation that halide oxidation indeed plays a key role in halide segregation.

The schematics in Figure 10 show a simplification of the segregation process step by step. In short, first, the iodide (purple) is oxidized by the incoming irradiation, leading to a higher iodine mobility. The band gap differences and lattice strain give the condition for phase segregation and preferential direction for the fast moving iodine, while the bromide (brown) follows via slower processes to satisfy the stoichiometry and release of lattice strain.

The simplified view in Figure 10 shows only the halides of the initially I-rich (upper row) and Br-rich (lower row) mixed-halides. The initial mixed state under equilibrium conditions is depicted at the left.

Step 1: The incoming electromagnetic field (electron beam or light) excites an electron from the valence-band to the conduction-band.[38] The valence-band maximum consists of a halide orbital.[70] The induced hole densities lead to the oxidation of the halide anion and subsequently result in the breaking of the X−Pb bond. Because the oxidation potential E^O is higher for Br than for I, I is oxidized preferentially. The oxidation potential E^O for the formation of molecular iodide or bromide via $2X^- \rightarrow 2X_2^0 + 2e^-$, is $E_I^O = +0.535$ V and $E_{Br}^O = +1.065$ V.[22,24,71] Therefore, chemically, the oxidation of bromide is not relevant, as long as there is iodide to oxidize. This also rationalizes the reported expulsion of iodide,[22−24] even though kinetically, Br^0, Br^-, or Br_2 should all be more mobile due to their smaller radius than I^0, I^-, or I_2.[72,73] The oxidation of iodide is a reversible redox reaction (oxidation: $2I^- \rightarrow 2I + 2e^-$; reduction: $Pb^{2+} + 2e^- \rightarrow Pb^0$; redox reaction: $2I^- + Pb^{2+} \rightarrow 2I + 2Pb^0$). However, the reversibility is dependent on the spatial distribution of the oxidized products after the initial process.[24]

The oxidation is the fundamental origin of the halide phase segregation and explains why the iodine is more mobile and moves further. Due to this oxidation process it is rather iodide,

https://doi.org/10.1021/acsmaterialsau.3c00056
ACS Mater. Au 2023, 3, 687−698

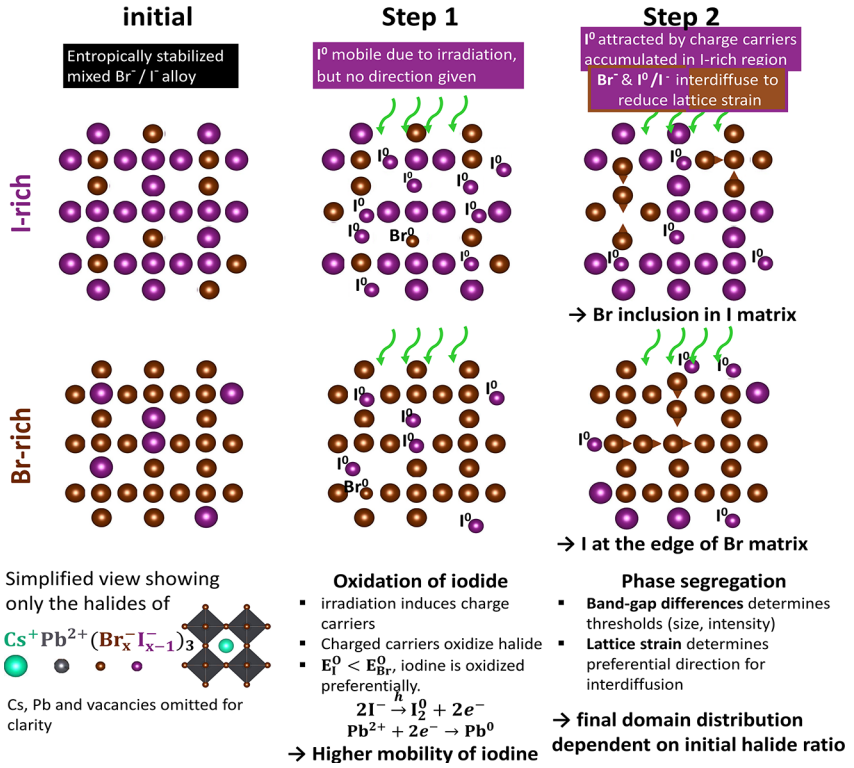

Figure 10. Schematics of proposed mechanism for halide phase segregation in initially I-rich and Br-rich LHP.

than bromide that outgases for NPs smaller than 23 nm, causing the blue shift of the PL peak. However, iodide oxidation alone cannot rationalize the preferential direction that is necessary for segregation to occur. Furthermore, the present work shows that not only the oxidized iodine but also the Br diffuses in NPs with sizes >40 nm. Iodine (whether in its radical I^0 or molecular I_2 form cannot be told from the present results) may move interstitially mediated[22] or diffuse via vacancies.[26,73] Vacancies can be assumed to be present from the beginning. The faster diffusion of iodide in comparison to bromide causes the occurrence of a Kirkendall effect, leading to the formation of further vacancies. This situation facilitates the interdiffusion via vacancy-mediated processes following the movement of the iodine to satisfy the stoichiometry.

Step 2: As a condition for halide phase segregation, the threshold values for excitation intensity and particle size also observed in the present work have to be surpassed. This can be explained by the band gap-based model, which is dependent on the excitation intensity I_{exc} as well as on the carrier diffusion length $L_{e/h}$.[9] The differences in band gap energies between I-rich and Br-rich regions cause charge-carrier accumulation in I-rich domains, which again causes the mobile iodine to diffuse to these regions.

To explain the preferential direction in dependence of the initial halide ratio, depicted in Figure 10, the following mechanism is proposed. While the I-rich compound turns into a $CsPbI_3$ matrix with small Br-rich inclusions, for the Br-rich sample, a $CsPbBr_3$ domain forms in the center, while iodine segregates to the edges. The common element of the spatial evolution starting from the two different initial [Br]:[I] ratios in the crystallites with sizes of >40 nm is that the material systems tend to build up the pure $CsPbX_3$ phase of the predominant halide X. This supports our proposal that the following mechanism introduced in Funk et al.[50] drives the segregation: The difference in Shannon ionic radii for Br and I[74] result in an asymmetry in bonding strengths (see Table S2) and causes the lattice to be strained. The spatial evolution of the phases strongly suggests that, under the condition that the bromide is less mobile than the iodide, the systems seek strain-release by evolving into the pure phase of the predominant phase.

The interplay of three factors, iodine oxidation, differences in band gap energy and lattice strain, can rationalize the various results obtained in the present work. Furthermore, it explains why electron-beam and light irradiation can both trigger phase segregation in LHP compounds.

5. CONCLUSIONS

The present work investigated halide phase-segregation in nanocrystals of mixed-halide $CsPb(Br_xI_{1-x})_3$ in dependence on their sizes and their initial halide [Br]:[I] ratios. The segregation was induced and monitored in situ by HRTEM on the sub-nm level, and the results were correlated with light-induced phase segregation monitored by PL spectroscopy. From in situ HRTEM measurements of inorganic LHP NPs, a clear direction for electron-beam-induced phase segregation was observable in a Br-rich crystallite, where an I-rich phase segregated at the borders of the particle while a $CsPbBr_3$ domain formed at the center. In contrast, the I-rich crystallite becomes a $CsPbI_3$ matrix with small, Br-rich inclusions. PL analyses using light irradiation on the identical sample indicated the same phase segregation to pure $CsPbI_3$. No phase segregation was observed by HRTEM or PL in particles of side length of ≤22 nm, confirming an NP size threshold below which no phase segregation takes place. However, the PL peaks acquired on NPs with side lengths of ≤22 nm

https://doi.org/10.1021/acsmaterialsau.3c00056
ACS Mater. Au 2023, 3, 687−698

exhibited a blue-shift of about 3 nm, indicating the loss of iodine.

The presented results show that to rationalize halide phase segregation, the interaction of three partial processes has to be considered. (1) Irradiation-induced iodide oxidation results in higher mobility of iodine than bromide. In combination with this process, (2) intrinsic differences in band gap energy explain the size and intensity thresholds below which no phase segregation but instead iodine expulsion occurs, and (3) intrinsic lattice strain provides the preferential direction in dependence of the initial halide ratio. Furthermore, since the oxidation can be induced by both electron-beam and light irradiation, both radiation sources can trigger phase segregation in LHP compounds.

■ ASSOCIATED CONTENT

Supporting Information

The Supporting Information is available free of charge at https://pubs.acs.org/doi/10.1021/acsmaterialsau.3c00056.

> Literature overview of PL peaks for different halide ratios in $CsPb(Br_xI_{1-x})_3$; calculated bonding lengths for $CsPbBr_3$ and $CsPbI_3$; interplanar spacings for $CsPbBr_3$, $CsPbI_3$; $PbBr_2$, PbI_2, and Pb; further absorption and PL measurements; additional HRTEM time series with corresponding MA abundance maps; HRTEMs with more detailed phase assignment; details on the influence of residual organic material including HRTEM and low-magnification TEM images; detailed analysis of heat effects in the electron beam (PDF)

■ AUTHOR INFORMATION

Corresponding Author

Daniel Abou-Ras − *Helmholtz-Zentrum Berlin für Materialien und Energie GmbH, 14109 Berlin, Germany;* orcid.org/0000-0003-3063-922X; Email: daniel.abou-ras@helmholtz-berlin.de

Authors

Hannah Funk − *Helmholtz-Zentrum Berlin für Materialien und Energie GmbH, 14109 Berlin, Germany;* orcid.org/0000-0001-9796-2350

Tal Binyamin − *The Institute of Chemistry, The Center for Nanoscience and Nanotechnology, The Casali Center for Applied Chemistry, The Hebrew University of Jerusalem, Jerusalem 9190401, Israel*

Lioz Etgar − *The Institute of Chemistry, The Center for Nanoscience and Nanotechnology, The Casali Center for Applied Chemistry, The Hebrew University of Jerusalem, Jerusalem 9190401, Israel*

Oleksandra Shargaieva − *Helmholtz-Zentrum Berlin für Materialien und Energie GmbH, 14109 Berlin, Germany*

Thomas Unold − *Helmholtz-Zentrum Berlin für Materialien und Energie GmbH, 14109 Berlin, Germany;* orcid.org/0000-0002-5750-0693

Alberto Eljarrat − *Humboldt-Universität zu Berlin, Institut für Physik, 12489 Berlin, Germany;* orcid.org/0000-0002-0968-5195

Christoph T. Koch − *Humboldt-Universität zu Berlin, Institut für Physik, 12489 Berlin, Germany;* orcid.org/0000-0002-3984-1523

Complete contact information is available at: https://pubs.acs.org/10.1021/acsmaterialsau.3c00056

Author Contributions

The manuscript was written through contributions by all authors. All authors have given approval to the final version of the manuscript.

Notes

The authors declare no competing financial interest.

■ ACKNOWLEDGMENTS

The authors are grateful for the financial support of the Helmholtz International Research School HISCORE (HIRS-0008) and of the HyPerCells Research School. L.E. and T.B. thank the Israel Science Foundation grant no. 937/18 for the financial support. O.S. acknowledges funding from the German Science Foundation (DFG) provided in the framework of the priority program SPP 2196, "Perovskite semiconductors: From fundamental properties to devices" Project number 424394788. C.T.K. and A.E. acknowledge financial support by the German Research Foundation (DFG, project number 182087777 - SFB951).

■ REFERENCES

(1) Egger, D. A.; Bera, A.; Cahen, D.; Hodes, G.; Kirchartz, T.; Kronik, L.; Lovrincic, R.; Rappe, A. M.; Reichman, D. R.; Yaffe, O. What Remains Unexplained about the Properties of Halide Perovskites? *Adv. Mater.* **2018**, *30*, 1800691.

(2) Saliba, M.; Correa-Baena, J. P.; Grätzel, M.; Hagfeldt, A.; Abate, A. Perovskite Solar Cells: From the Atomic Level to Film Quality and Device Performance. *Angew. Chem., Int. Ed.* **2018**, *57*, 2554−2569.

(3) NREL. *Interactive Best Research-Cell Efficiency Chart*, https://www.nrel.gov/pv/interactive-cell-efficiency.html (accessed Aug 28, 2023).

(4) Al-Ashouri, A.; Köhnen, E.; Li, B.; Magomedov, A.; Hempel, H.; Caprioglio, P.; Márquez, J. A.; Morales Vilches, A. B.; Kasparavicius, E.; Smith, J. A.; Phung, N.; Menzel, D.; Grischek, M.; Kegelmann, L.; Skroblin, D.; Gollwitzer, C.; Malinauskas, T.; Jošt, M.; Matič, G.; Rech, B.; Schlatmann, R.; Topič, M.; Korte, L.; Abate, A.; Stannowski, B.; Neher, D.; Stolterfoht, M.; Unold, T.; Getautis, V.; Albrecht, S. Monolithic Perovskite/Silicon Tandem Solar Cell with >29% Efficiency by Enhanced Hole Extraction. *Science* **2020**, *370*, 1300−1309.

(5) Hoke, E. T.; Slotcavage, D. J.; Dohner, E. R.; Bowring, A. R.; Karunadasa, H. I.; McGehee, M. D. Reversible Photo-Induced Trap Formation in Mixed-Halide Hybrid Perovskites for Photovoltaics. *Chem. Sci.* **2015**, *6*, 613−617.

(6) Ravi, V. K.; Markad, G. B.; Nag, A. Band Edge Energies and Excitonic Transition Probabilities of Colloidal CsPbX3 (X = Cl, Br, I) Perovskite Nanocrystals. *ACS Energy Lett.* **2016**, *1*, 665−671.

(7) Beal, R. E.; Slotcavage, D. J.; Leijtens, T.; Bowring, A. R.; Belisle, R. A.; Nguyen, W. H.; Burkhard, G. F.; Hoke, E. T.; McGehee, M. D. Cesium Lead Halide Perovskites with Improved Stability for Tandem Solar Cells. *J. Phys. Chem. Lett.* **2016**, *7*, 746−751.

(8) Unger, E. L.; Kegelmann, L.; Suchan, K.; Sörell, D.; Korte, L.; Albrecht, S. Roadmap and Roadblocks for the Band Gap Tunability of Metal Halide Perovskites. *J. Mater. Chem. A* **2017**, *5*, 11401−11409.

(9) Draguta, S.; Sharia, O.; Yoon, S. J.; Brennan, M. C.; Morozov, Y. V.; Manser, J. S.; Kamat, P. V.; Schneider, W. F.; Kuno, M. Rationalizing the Light-Induced Phase Separation of Mixed Halide Organic-Inorganic Perovskites. *Nat. Commun.* **2017**, *8*, 200.

(10) Gualdrón-Reyes, A. F.; Yoon, S. J.; Barea, E. M.; Agouram, S.; Muñoz-Sanjosé, V.; Meléndez, Á. M.; Niño-Gómez, M. E.; Mora-Seró, I. Controlling the Phase Segregation in Mixed Halide Perovskites through Nanocrystal Size. *ACS Energy Lett.* **2019**, *4*, 54−62.

(11) Wang, X.; Ling, Y.; Lian, X.; Xin, Y.; Dhungana, K. B.; Perez-Orive, F.; Knox, J.; Chen, Z.; Zhou, Y.; Beery, D.; Hanson, K.; Shi, J.; Lin, S.; Gao, H. Suppressed Phase Separation of Mixed-Halide Perovskites Confined in Endotaxial Matrices. *Nat. Commun.* **2019**, *10*, 1−7.
(12) Bischak, C. G.; Hetherington, C. L.; Wu, H.; Aloni, S.; Ogletree, D. F.; Limmer, D. T.; Ginsberg, N. S. Origin of Reversible Photoinduced Phase Separation in Hybrid Perovskites. *Nano Lett.* **2017**, *17*, 1028−1033.
(13) Brennan, M. C.; Ruth, A.; Kamat, P. V.; Kuno, M. Photoinduced Anion Segregation in Mixed Halide Perovskites. *Trends Chem.* **2020**, *2*, 282−301.
(14) Brivio, F.; Caetano, C.; Walsh, A. Thermodynamic Origin of Photoinstability in the CH3NH3Pb(I1-XBrx)3 Hybrid Halide Perovskite Alloy. *J. Phys. Chem. Lett.* **2016**, *7*, 1083−1087.
(15) Hutter, E. M.; Muscarella, L. A.; Wittmann, F.; Versluis, J.; McGovern, L.; Bakker, H. J.; Woo, Y. W.; Jung, Y. K.; Walsh, A.; Ehrler, B. Thermodynamic Stabilization of Mixed-Halide Perovskites against Phase Segregation. *Cell Rep. Phys. Sci.* **2020**, *1*, No. 100120.
(16) Suchan, K.; Merdasa, A.; Rehermann, C.; Unger, E. L.; Scheblykin, I. G. Complex Evolution of Photoluminescence during Phase Segregation of MAPb(I1-XBrx)3 Mixed Halide Perovskite. *J. Lumin.* **2020**, *221*, No. 117073.
(17) Suchan, K.; Just, J.; Beblo, P.; Rehermann, C.; Merdasa, A.; Mainz, R.; Scheblykin, I. G.; Unger, E. Multi-Stage Phase-Segregation of Mixed Halide Perovskites under Illumination: A Quantitative Comparison of Experimental Observations and Thermodynamic Models. *Adv. Funct. Mater.* **2023**, *33*, 2206047.
(18) Ehrler, B.; Hutter, E. M. Routes toward Long-Term Stability of Mixed-Halide Perovskites. *Matter* **2020**, *2*, 800−802.
(19) Samu, G. F.; Balog, Á.; De Angelis, F.; Meggiolaro, D.; Kamat, P. V.; Janáky, C. Electrochemical Hole Injection Selectively Expels Iodide from Mixed Halide Perovskite Films. *J. Am. Chem. Soc.* **2019**, *141*, 10812−10820.
(20) Kim, G. Y.; Senocrate, A.; Yang, T. Y.; Gregori, G.; Grätzel, M.; Maier, J. Large Tunable Photoeffect on Ion Conduction in Halide Perovskites and Implications for Photodecomposition. *Nat. Mater.* **2018**, *17*, 445−449.
(21) Zhang, H.; Fu, X.; Tang, Y.; Wang, H.; Zhang, C.; Yu, W. W.; Wang, X.; Zhang, Y.; Xiao, M. Phase Segregation Due to Ion Migration in All-Inorganic Mixed-Halide Perovskite Nanocrystals. *Nat. Commun.* **2019**, *10*, 1−8.
(22) Frolova, L. A.; Luchkin, S. Y.; Lekina, Y.; Gutsev, L. G.; Tsarev, S. A.; Zhidkov, I. S.; Kurmaev, E. Z.; Shen, Z. X.; Stevenson, K. J.; Aldoshin, S. M.; Troshin, P. A. Reversible Pb2+/Pb0 and I−/I3− Redox Chemistry Drives the Light-Induced Phase Segregation in All-Inorganic Mixed Halide Perovskites. *Adv. Energy Mater.* **2021**, *11*, 1−11.
(23) Mathew, P. S.; Samu, G. F.; Janáky, C.; Kamat, P. V. Iodine (I) Expulsion at Photoirradiated Mixed Halide Perovskite Interface. *Should i Stay or Should i Go? ACS Energy Lett.* **2020**, *5*, 1872−1880.
(24) Kerner, R. A.; Xu, Z.; Larson, B. W.; Rand, B. P. The Role of Halide Oxidation in Perovskite Halide Phase Separation. *Joule* **2021**, *5*, 2273−2295.
(25) Tiede, D. O.; Calvo, M. E.; Galisteo-López, J. F.; Míguez, H. Local Rearrangement of the Iodide Defect Structure Determines the Phase Segregation Effect in Mixed-Halide Perovskites. *J. Phys. Chem. Lett.* **2020**, *11*, 4911−4916.
(26) Kamat, P. V.; Kuno, M. Halide Ion Migration in Perovskite Nanocrystals and Nanostructures. *Acc. Chem. Res.* **2021**, *54*, 520−531.
(27) Kim, G. Y.; Senocrate, A.; Wang, Y. R.; Moia, D.; Maier, J. Photo-Effect on Ion Transport in Mixed Cation and Halide Perovskites and Implications for Photo-Demixing. *Angew. Chem., Int. Ed.* **2021**, *60*, 820−826.
(28) Klein-Kedem, N.; Cahen, D.; Hodes, G. Effects of Light and Electron Beam Irradiation on Halide Perovskites and Their Solar Cells. *Acc. Chem. Res.* **2016**, *49*, 347−354.
(29) Egerton, R. F.; Crozier, P. A.; Rice, P. Electron Energy-Loss Spectroscopy and Chemical Change. *Ultramicroscopy* **1987**, *23*, 305−312.
(30) Egerton, R. F.; Li, P.; Malac, M. Radiation Damage in the TEM and SEM. *Micron* **2004**, *35*, 399−409.
(31) Egerton, R. F. Mechanisms of Radiation Damage in Beam-Sensitive Specimens, for TEM Accelerating Voltages between 10 and 300 KV. *Microsc. Res. Tech.* **2012**, *75*, 1550−1556.
(32) Egerton, R. F. Control of Radiation Damage in the TEM. *Ultramicroscopy* **2013**, *127*, 100−108.
(33) Egerton, R. F. Beam-Induced Motion of Adatoms in the Transmission Electron Microscope. *Microsc. Microanal.* **2013**, *19*, 479−486.
(34) Egerton, R. F. Radiation Damage to Organic and Inorganic Specimens in the TEM. *Micron* **2019**, *119*, 72−87.
(35) Dang, Z.; Shamsi, J.; Akkerman, Q. A.; Imran, M.; Bertoni, G.; Brescia, R.; Manna, L. Low-Temperature Electron Beam-Induced Transformations of Cesium Lead Halide Perovskite Nanocrystals. *ACS Omega* **2017**, *2*, 5660−5665.
(36) Dang, Z.; Shamsi, J.; Palazon, F.; Imran, M.; Akkerman, Q. A.; Park, S.; Bertoni, G.; Prato, M.; Brescia, R.; Manna, L. *In Situ* Transmission Electron Microscopy Study of Electron Beam-Induced Transformations in Colloidal Cesium Lead Halide Perovskite Nanocrystals. *ACS Nano* **2017**, *11*, 2124−2132.
(37) Dang, Z.; Luo, Y.; Wang, X.-S.; Imran, M.; Gao, P. Electron-Beam-Induced Degradation of Halide-Perovskite-Related Semiconductor Nanomaterials. *Chin. Opt. Lett.* **2021**, *19*, No. 030002.
(38) Dang, Z.; Luo, Y.; Xu, Y.; Gao, P.; Wang, X.-S. Transformation and Degradation of Metal Halide Perovskites Induced by Energetic Electrons and Their Practical Implications. *Nano Futures* **2021**, *5*, No. 032001.
(39) Chen, X.; Wang, Z. Investigating Chemical and Structural Instabilities of Lead Halide Perovskite Induced by Electron Beam Irradiation. *Micron* **2019**, *116*, 73−79.
(40) Chen, S.; Gao, P. Challenges, Myths, and Opportunities of Electron Microscopy on Halide Perovskites. *J. Appl. Phys.* **2020**, *128*, No. 010901.
(41) Chen, S.; Zhang, Y.; Zhao, J.; Mi, Z.; Zhang, J.; Cao, J.; Feng, J.; Zhang, G.; Qi, J.; Li, J.; Gao, P. Transmission Electron Microscopy of Organic-Inorganic Hybrid Perovskites: Myths and Truths. *Sci. Bull.* **2020**, *65*, 1643−1649.
(42) Williams, D. B.; Carter, C. B. Transmission Electron Microscopy: *A Textbook for Materials Science*; 2009, DOI: 10.1007/978-0-387-76501-3.
(43) Rothmann, M. U.; Li, W.; Zhu, Y.; Liu, A.; Ku, Z.; Bach, U.; Etheridge, J.; Cheng, Y.-B. Structural and Chemical Changes to $CH_3NH_3PbI_3$ Induced by Electron and Gallium Ion Beams. *Adv. Mater.* **2018**, *30*, 1800629.
(44) Alberti, A.; Bongiorno, C.; Smecca, E.; Deretzis, I.; La Magna, A.; Spinella, C. Pb Clustering and PbI2 Nanofragmentation during Methylammonium Lead Iodide Perovskite Degradation. *Nat. Commun.* **2019**, *10*, 2196.
(45) Song, K.; Liu, L.; Zhang, D.; Hautzinger, M. P.; Jin, S.; Han, Y. Atomic-Resolution Imaging of Halide Perovskites Using Electron Microscopy. *Adv. Energy Mater.* **2020**, *10*, 1904006.
(46) Ran, J.; Dyck, O.; Wang, X.; Yang, B.; Geohegan, D. B.; Xiao, K. Electron-Beam-Related Studies of Halide Perovskites: Challenges and Opportunities. *Adv. Energy Mater.* **2020**, *10*, 1903191.
(47) Chen, S.; Zhang, Y.; Zhang, X.; Zhao, J.; Zhao, Z.; Su, X.; Hua, Z.; Zhang, J.; Cao, J.; Feng, J.; Wang, X.; Li, X.; Qi, J.; Li, J.; Gao, P. General Decomposition Pathway of Organic−Inorganic Hybrid Perovskites through an Intermediate Superstructure and Its Suppression Mechanism. *Adv. Mater.* **2020**, *32*, 2001107.
(48) Deng, Y. H. Common Phase and Structure Misidentifications in High-Resolution Tem Characterization of Perovskite Materials. *Condens. Matter* **2021**, *6*, 1−8.
(49) Kosasih, F. U.; Cacovich, S.; Divitini, G.; Ducati, C. Nanometric Chemical Analysis of Beam-Sensitive Materials: A Case

Study of STEM-EDX on Perovskite Solar Cells. *Small Methods* **2021**, *5*, 2000835.
(50) Funk, H.; Shargaieva, O.; Eljarrat, A.; Unger, E. L.; Koch, C. T.; Abou-Ras, D. In Situ TEM Monitoring of Phase-Segregation in Inorganic Mixed Halide Perovskite. *J. Phys. Chem. Lett.* **2020**, *11*, 4945−4950.
(51) Funk, H. Microscopic Insights into Phases and Their Transformations in Inorganic Halide Perovskites. *Tech. Univ. Berlin* **2022**, DOI: 10.14279/depositonce-15097.
(52) Protesescu, L.; Yakunin, S.; Bodnarchuk, M. I.; Krieg, F.; Caputo, R.; Hendon, C. H.; Yang, R. X.; Walsh, A.; Kovalenko, M. V. Nanocrystals of Cesium Lead Halide Perovskites (CsPbX3, X = Cl, Br, and I): Novel Optoelectronic Materials Showing Bright Emission with Wide Color Gamut. *Nano Lett.* **2015**, *15*, 3692−3696.
(53) Pearson. LIII. On Lines and Planes of Closest Fit to Systems of Points in Space. *London, Edinburgh, Dublin Philos. Mag. J. Sci.* **1901**, *2*, 559−572.
(54) Jutten, C.; Herault, J. Blind Separation of Sources, Part I: An Adaptive Algorithm Based on Neuromimetic Architecture. *Signal Process.* **1991**, *24*, 1−10.
(55) Abou-Ras, D.; Bloeck, U.; Caicedo-Dávila, S.; Eljarrat, A.; Funk, H.; Hammud, A.; Thomas, S.; Wargulski, D. R.; Lunkenbein, T.; Koch, C. T. Correlative Microscopy and Monitoring of Segregation Processes in Optoelectronic Semiconductor Materials and Devices. *J. Appl. Phys.* **2023**, *133*, 121101.
(56) Zhang, Q.; Su, R.; Liu, X.; Xing, J.; Sum, T. C.; Xiong, Q. High-Quality Whispering-Gallery-Mode Lasing from Cesium Lead Halide Perovskite Nanoplatelets. *Adv. Funct. Mater.* **2016**, *26*, 6238−6245.
(57) Nedelcu, G.; Protesescu, L.; Yakunin, S.; Bodnarchuk, M. I.; Grotevent, M. J.; Kovalenko, M. V. Fast Anion-Exchange in Highly Luminescent Nanocrystals of Cesium Lead Halide Perovskites (CsPbX3, X = Cl, Br, I). *Nano Lett.* **2015**, *15*, 5635−5640.
(58) Chen, Q.; Wu, J.; Ou, X.; Huang, B.; Almutlaq, J.; Zhumekenov, A. A.; Guan, X.; Han, S.; Liang, L.; Yi, Z.; Li, J.; Xie, X.; Wang, Y.; Li, Y.; Fan, D.; Teh, D. B. L.; All, A. H.; Mohammed, O. F.; Bakr, O. M.; Wu, T.; Bettinelli, M.; Yang, H.; Huang, W.; Liu, X. All-Inorganic Perovskite Nanocrystal Scintillators. *Nature* **2018**, *561*, 88−93.
(59) Bi, C.; Kershaw, S. V.; Rogach, A. L.; Tian, J. Improved Stability and Photodetector Performance of CsPbI3 Perovskite Quantum Dots by Ligand Exchange with Aminoethanethiol. *Adv. Funct. Mater.* **2019**, *29*, 1−9.
(60) Brennan, M. C.; Draguta, S.; Kamat, P. V.; Kuno, M. Light-Induced Anion Phase Segregation in Mixed Halide Perovskites. *ACS Energy Lett.* **2018**, *3*, 204−213.
(61) Staub, F.; Anusca, I.; Lupascu, D. C.; Rau, U.; Kirchartz, T. Effect of Reabsorption and Photon Recycling on Photoluminescence Spectra and Transients in Lead-Halide Perovskite Crystals. *J. Phys. Mater.* **2020**, *3*, No. 025003.
(62) Vegard, L. Die Konstitution Der Mischkristalle Und Die Raumfüllung Der Atome. *Z. Phys.* **1921**, *5*, 17−26.
(63) Møller, C. K. Crystal Structure and Photoconductivity of Caesium Plumbohalides. *Nature* **1958**, *182*, 1436.
(64) Trots, D. M.; Myagkota, S. V. High-Temperature Structural Evolution of Caesium and Rubidium Triiodoplumbates. *J. Phys. Chem. Solids* **2008**, *69*, 2520−2526.
(65) Bertolotti, F.; Protesescu, L.; Kovalenko, M. V.; Yakunin, S.; Cervellino, A.; Billinge, S. J. L.; Terban, M. W.; Pedersen, J. S.; Masciocchi, N.; Guagliardi, A. Coherent Nanotwins and Dynamic Disorder in Cesium Lead Halide Perovskite Nanocrystals. *ACS Nano* **2017**, *11*, 3819−3831.
(66) Deng, Y. H.; Nest, L. G. Analysis of Misidentifications in TEM Characterisation of Organic-Inorganic Hybrid Perovskite Material. *J. Microsc.* **2021**, *282*, 195−204.
(67) Stadelmann, P. A. *JEMS Electron Microscopy Software*, Java Version 4.6131U2018, JEMS-SAAS: Switzerland.
(68) Chen, Z.; Brocks, G.; Tao, S.; Bobbert, P. A. Unified Theory for Light-Induced Halide Segregation in Mixed Halide Perovskites. *Nat. Commun.* **2021**, *12*, 2687.
(69) Scheidt, R. A.; Atwell, C.; Kamat, P. V. Tracking Transformative Transitions: From $CsPbBr_3$ Nanocrystals to Bulk Perovskite Films. *ACS Mater. Lett.* **2019**, *1*, 8−13.
(70) Unger, E. L.; Shargaieva, O.; Braunger, S.; Docampo, P.Solution-processed Solar Cells: Perovskite Solar Cells In *Solar Energy Capture Materials* The Royal Society of Chemistry 2019, 153-192, DOI: 10.1039/9781788013512-00153.
(71) Greenwood, N. N.; Earnshaw, A. *Chemistry of the Elements (2nd Edition)*; 1997.
(72) Yuan, Y.; Wang, Q.; Huang, J. Ion Migration in Hybrid Perovskite Solar Cells. In *Organic-Inorganic Halide Perovskite Photovoltaics*; Springer International Publishing Cham, 2016; pp. 137−162, DOI: 10.1007/978-3-319-35114-8_6.
(73) Barker, A. J.; Sadhanala, A.; Deschler, F.; Gandini, M.; Senanayak, S. P.; Pearce, P. M.; Mosconi, E.; Pearson, A. J.; Wu, Y.; Srimath Kandada, A. R.; Leijtens, T.; De Angelis, F.; Dutton, S. E.; Petrozza, A.; Friend, R. H. Defect-Assisted Photoinduced Halide Segregation in Mixed-Halide Perovskite Thin Films. *ACS Energy Lett.* **2017**, *2*, 1416−1424.
(74) Shannon, R. D. Revised Effective Ionic Radii and Systematic Studies of Interatomic Distances in Halides and Chalcogenides. *Acta Crystallogr., Sect. A: Cryst. Phys., Diffr., Theor. Gen. Crystallogr.* **1976**, *32*, 751−767.

https://doi.org/10.1021/acsmaterialsau.3c00056
ACS Mater. Au 2023, 3, 687−698